NANO LETTERS

Letter

pubs.acs.org/NanoLett

Manipulating Surface States of III–V Nanowires with Uniaxial Stress

G. Signorello,*[,†] S. Sant,[‡] N. Bologna,[§] M. Schraff,[†] U. Drechsler,[†] H. Schmid,[†] S. Wirths,[†] M. D. Rossell,[§] A. Schenk,[‡] and H. Riel[†]

[†]IBM Research - Zurich, 8803 Rüschlikon, Switzerland

[‡]Integrated Systems Laboratory, Department of Electrical Engineering and Information Technology, ETH Zürich, 8092 Zürich, Switzerland

[§]Electron Microscopy Center, EMPA, Swiss Federal Laboratories for Materials Science and Technology, 8600 Dübendorf, Switzerland

Supporting Information

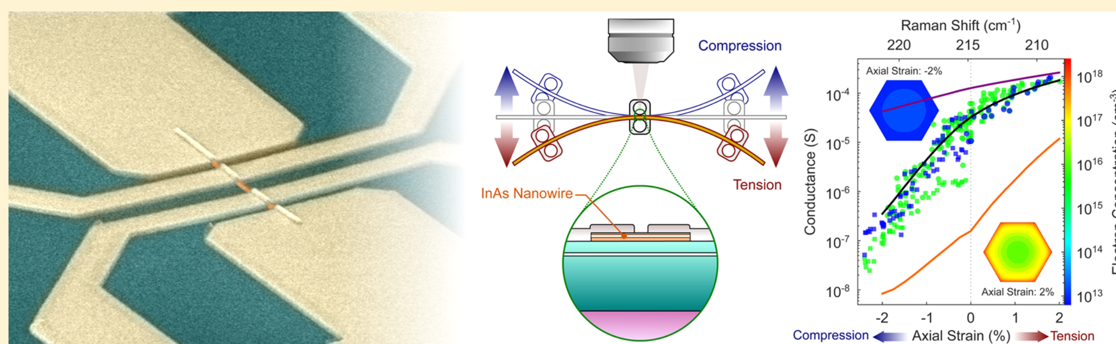

ABSTRACT: III–V compound semiconductors are indispensable materials for today's high-end electronic and optoelectronic devices and are being explored for next-generation transistor logic and quantum technologies. III–V surfaces and interfaces play the leading role in determining device performance, and therefore, methods to control their electronic properties have been developed. Typically, surface passivation studies demonstrated how to limit the density of surface states. Strain has been widely used to improve the electronic transport properties and optoelectronic properties of III–Vs, but the potential of this technology to modify the surface properties still remains to be explored. Here we show that uniaxial stress induces a shift in the energy of the surface states of III–V nanowires, modifying their electronic properties. We demonstrate this phenomenon by modulating the conductivity of InAs nanowires over 4 orders of magnitude with axial strain ranging between −2.5% in compression and 2.1% in tension. The band bending at the surface of the nanostructure is modified from accumulation to depletion reversibly and reproducibly. We provide evidence of this physical effect using a combination of electrical transport measurement, Raman spectroscopy, band-structure modeling, and technology computer aided design (TCAD) simulations. With this methodology, the deformation potentials for the surface states are quantified. These results reveal that strain technology can be used to shift surface states away from energy ranges in which device performance is negatively affected and represent a novel route to engineer the electronic properties of III–V devices.

KEYWORDS: *Uniaxial stress, InAs nanowire, surface accumulation, surface states, charge modulation, giant gauge-factor*

The III–V compound semiconductors are promising materials to enable continued scaling for the next generation of transistor technology[1−6] and are the subject of intense research for integrating lasers on silicon,[7−9] for sensing applications,[10,11] for energy harvesting,[12,13] and for quantum technologies.[14−18] In particular InAs is an attractive material because of its small effective mass and an electron mobility that is ten times larger than that of silicon. It is being investigated for low-power complementary metal–oxide–semiconductor (CMOS) applications at supply voltages smaller than 0.5 V[19,20] and was used to demonstrate that its high injection velocity can be maintained also in aggressively scaled devices.[21,22]

The interesting electron-transport properties of InAs, however, are also related to the small density of states in the conduction band. As a positive bias is applied to the surface of InAs, the Fermi level can shift all the way into the conduction band, where the effects of traps and interface states can be significant. Unlike silicon and its native oxide, III–V alloys do not have stable oxide surfaces free from ionized defects. The details of III–V surfaces and interfaces are therefore critical for device performance.[23−25] InGaAs MOS interfaces have been shown to have acceptor-type defects in proximity to or in the

Received: December 8, 2016
Revised: April 6, 2017
Published: April 6, 2017

 © 2017 American Chemical Society DOI: 10.1021/acs.nanolett.6b05098
Nano Lett. 2017, 17, 2816−2824

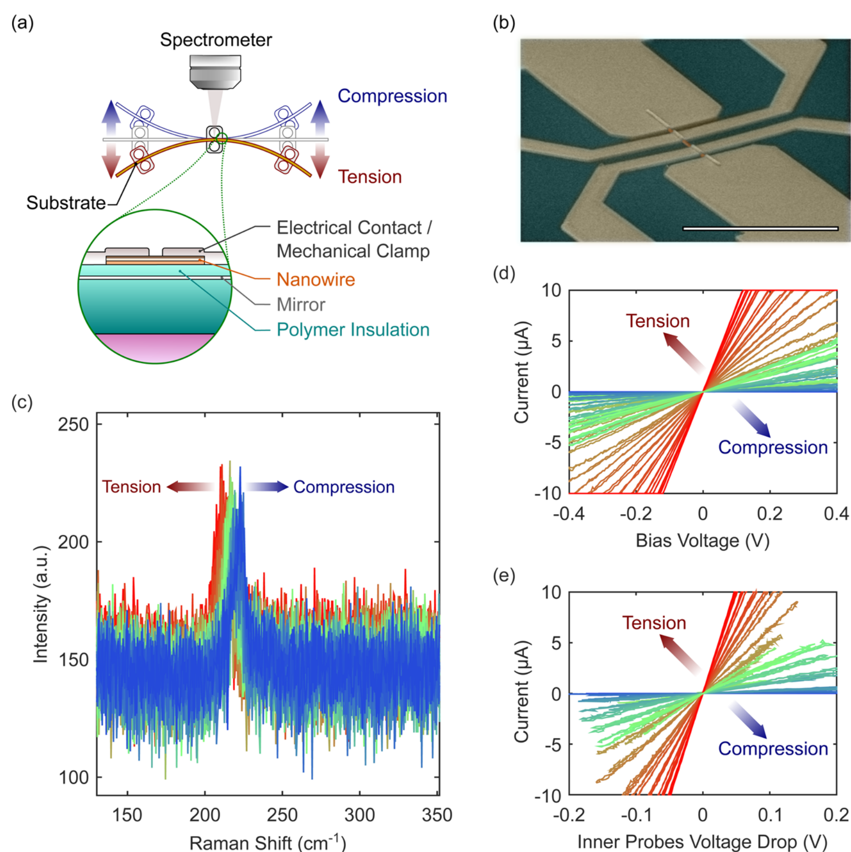

Figure 1. (a) Schematic representation of the experimental setup. Strain is applied to a nanowire structure by bending the substrate in a three-point geometry. Electrical transport and Raman spectroscopy are used to characterize the device. (b) False-color SEM micrograph of a strain InAs nanowire device, contacted in a four-probe geometry. The nanowire is shown in orange. The polymer substrate is indicated in teal. The scale bar is 5 μm long. (c) Effect of uniaxial stress on the Raman spectrum of the central segment of an InAs nanowire. Compressive stress (in blue) increases the optical phonon energy, whereas tensile stress (in red) decreases it compared with the unstrained condition (in green). (d) Two-probe and (e) four-probe electrical transport characteristics of an InAs nanowire subject to uniaxial stress. Tensile stress increases the conductivity of the nanowire, compressive stress suppresses it.

conduction band, whereas states in proximity of the valence band exhibit donor-type behavior.[26−28] In the case of InAs, the surface reconstruction is responsible for the existence of ionized interface states inside the conduction band, which leads to a strong charge accumulation at the surface.[29−31] Under these circumstances, the Fermi level is located at an energy close to the defect states and is said to be pinned in the conduction band.[32] Interface passivation studies have been performed to engineer the properties of the surface accumulation layer of InAs nanowires and demonstrated a significant reduction of the density of interface states compared with untreated surfaces.[23,33,34] Surface-specific experiments suggested that the InAs surface accumulation is sensitive to the surface orientation and reconstruction.[35,36] Following its successful application in silicon technology,[37−39] the effect of strain has been studied in III−V devices and has revealed the potential for performance enhancements in a wide class of III−V alloys[40] and future transistors.[41−43] The application of uniaxial strain on III−V transistors, however, showed that strain strongly influences the transistor's electrostatics and that this effect dominates over the enhancement of the pure transport characteristics.[44]

Semiconductor nanowires exhibit exceptional mechanical properties when their lateral dimensions are scaled below 100 nm.[45] The details of the mechanics of surfaces can differ significantly from those of bulk,[46] and, as a consequence, the compliance tensor and the yield strength can be modified by scaling the nanowire cross section.[47,48] By leveraging these phenomena, record high values of strain were achieved,[49] and novel insights into the band-structure properties were gained.[50,51] Notably, a surprisingly large change in resistance with stress was measured on semiconducting nanowires, but the physical origin of this phenomenon has remained controversial.[52−55] A remarkable piezo-resistance was also demonstrated on InAs nanowires subjected to large stress.[56] This observation is in sharp contrast to what is expected for bulk InAs[57] and any material with conduction bands of spherical symmetry.[58] However, the complexity of the experiment and the limits in the fabrication process permitted only to establish Schottky contacts to the nanostructure.[59−61] Thus, the change in transport properties was dominated by the modulation of the barrier height induced by piezo-electric effects. Until today, the effect of high uniaxial stress on the surface properties of InAs and other III−V nanowires has remained unclear. In this Letter, we demonstrate that uniaxial stress modifies the surface properties and the electrical transport properties of InAs nanowires. We also provide insight into the shift in energy of the surface states.

Results. Individual InAs nanowire devices like the one shown in Figure 1b are realized on the surface of a flexible substrate.[62] Metal contacts to the device, fabricated by electron-beam lithography and lift-off technique, provide the electrical connection to the nanowire as well as the mechanical clamping

DOI: 10.1021/acs.nanolett.6b05098
Nano Lett. 2017, 17, 2816−2824

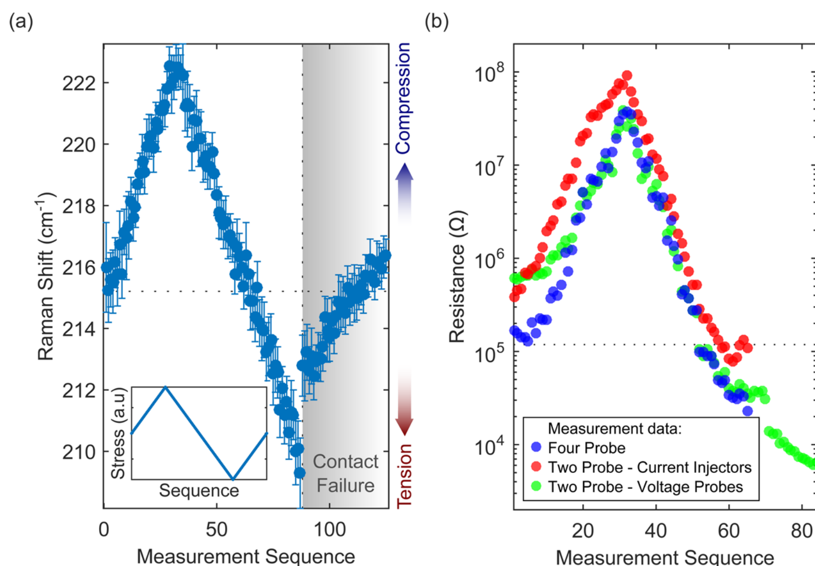

Figure 2. Analysis of the Raman spectrum and of the electrical measurements of an InAs nanowire subject to a stress cycle: (a) evolution of the TO phonon energy of the InAs nanowire upon applied stress profile. The sequence of stress values applied to the device, ranging from compression (applied first) to tension is shown in the inset. A discontinuity is observed for a tensile stress that shifts the TO phonon energy below the threshold of 208 cm^{-1}. (b) Evolution of the four-probe resistance (shown in blue), the two-probe resistance measured at the inner voltage probes (shown in green), and the two-probe resistance measured at the outer current injectors (shown in red). The values are shown only in the range in which all contacts necessary to perform a measurement are assessed as being functional.

to the substrate surface. The device is characterized by Raman spectroscopy and electrical transport while applying uniaxial stress, which is induced on the nanostructure by bending the substrate with a mechanical device sketched in Figure 1a. By bending the substrate in a three-point geometry, an extension or compression of the surface of the substrate is generated, and a part of it is coupled to the device under test by the mechanical clamps of the device. Uniaxial stress can be varied continuously from tension to compression by controlling the radius of curvature of the substrate and bending the substrate in convex or concave fashion, respectively.

When no stress is applied to the InAs nanowire, the Raman spectrum measured shows a single peak with an energy of (215.2 ± 1) cm^{-1}. This value of Raman shift corresponds well with the energy of the transversal optical (TO) phonon,[63,64] which is equal to 214.8 cm^{-1} in bulk zincblende InAs.[65,66] The electrical transport of the device is characterized using a four-probe configuration. The two outer probes, referred to as current injectors from now on, are connected to the voltage bias and to the ground contact. The two inner voltage probes enable the voltage drop between them to be measured without draining current. As expected for a device with ohmic metal−semiconductor contacts, the current−voltage ($I-V$) characteristics of the device is linear and characterized by a resistance of 300 kΩ. The four-probe resistance has a value of about of 200 kΩ and provides information about the intrinsic conductivity of the nanowire. To further confirm the ohmic nature of the metal−semiconductor interface, we imaged a cross section of the device at one of the current injectors using scanning transmission electron microscopy (STEM). The chemical analysis by energy dispersive X-ray spectroscopy (EDS) confirms that the InAs nanowire is alloyed with nickel under the metal contact region and provides strong confirmation of the ohmic nature of the metal−semiconductor interface (details are given in the Supporting Information, SI).

The results of the electrical and Raman spectroscopy characterizations of an InAs nanowire device, performed during a uniaxial stress cycle, are summarized in Figure 1c−e: the data shown in green were acquired without applied stress, those in blue were measured upon compression, and those in red were measured upon tension. Figure 1c shows that the Raman spectrum of the InAs nanowire shifts continuously upon stress over a very large range, from 208 cm^{-1} upon tension to 222 cm^{-1} upon compression. The intensity and the width of the Raman peak remain comparable across the entire stress range. Figure 1d shows the effect of uniaxial stress on the electrical-transport characteristics. The effect is remarkable: the current flowing through the nanowire device at a voltage bias of 400 mV varies from 5 μA in unstrained conditions to 32 μA for a maximum tensile stress (we limit its value to 10 μA by compliance) and to 4 nA for a maximum compressive stress. The $I-V$ characteristics remain linear throughout the entire stress cycle. An identical variation in conductivity over 4 orders of magnitude is also observed for the four-probe resistance. This is shown in Figure 1e, which plots the current flowing through the nanowire device as a function of the voltage drop between the inner probes. This observation provides solid evidence that the conductivity of the InAs nanowire is modulated by strain and is to be attributed to changes in the transport characteristics of the nanowire.

To gain a more detailed understanding of the phenomena occurring during the strain measurement summarized in Figure 1, we performed a nonlinear least-squares fitting of the Raman spectra and extracted the two-probe and four-probe differential resistances of the InAs device around zero bias voltage for every value of applied stress. The details of how the two stress measurements evolve are shown in Figure 2. The sequence of values of uniaxial stress applied to the InAs nanowire device, shown in the inset of Figure 2a, follows a triangular waveform. The corresponding values of the phonon peak position, estimated by fitting the Raman spectra for each value of

DOI: 10.1021/acs.nanolett.6b05098
Nano Lett. 2017, 17, 2816−2824

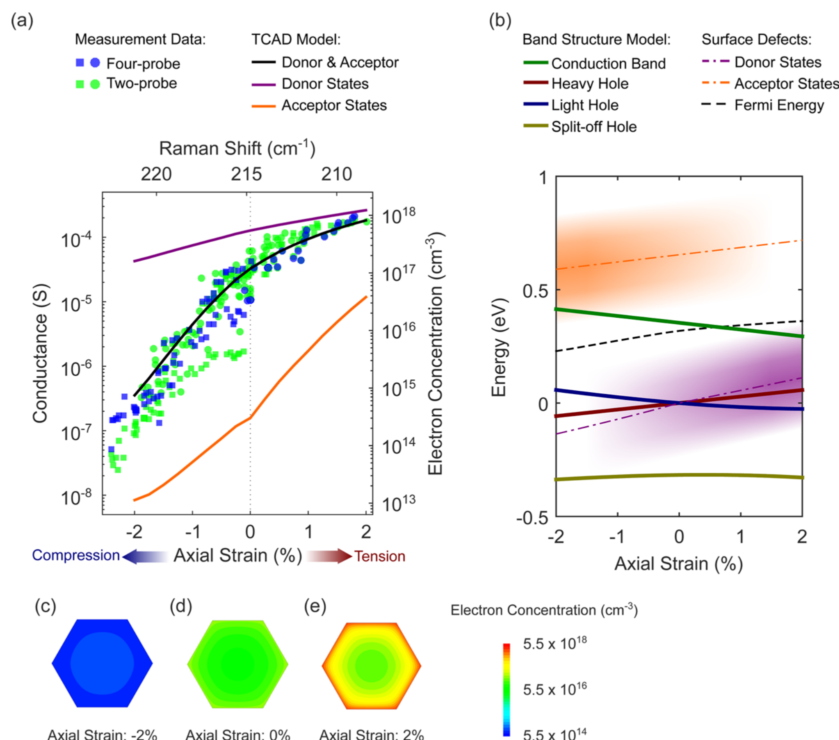

Figure 3. Characterization of the electrical transport of InAs nanowires as a function of strain and modeling with TCAD. (a) The four-probe resistance (blue data points) and two-probe resistance measured at the voltage probes (green data points) are plotted as a function of the InAs TO phonon energy (top axis), which is used to determine the axial strain in the nanowire (bottom axis). Circles and squares represent measurements on two distinct devices. The electron concentrations as modeled by TCAD are shown as continuous lines. The contribution of acceptor traps is shown in orange and that of donor traps in purple. Their joint effect is shown as a black solid line. (b) The uniaxial stress effect on the band structure of InAs is described using an 8-band k·p model. The energies of the acceptor and donor-trap distributions are inferred by a TCAD model. The shaded areas in proximity of the surface trap lines are a guide to the eye. A more intense color indicates a larger portion of ionized traps. The energy width of the shaded area indicates the full width at half-maximum of the surface trap distribution. The charge carrier distribution inside the nanowire cross section estimated (c) upon compression, (d) in unstrained conditions, and (e) upon tension are inferred by the TCAD model. Whereas surface accumulation is present in the unstrained condition and upon tensile stress, depletion is observed upon compression.

applied strain, are shown in Figure 2a. The energy shift of the Raman peak follows the applied stress waveform, increasing up to a value of (222.6 ± 0.6) cm^{-1} upon maximum compression and returning to its unstrained value upon removal of the compressive stress. The Raman spectra maintain a constant peak width of 4 cm^{-1} across the entire range of compressive stress (details are given in the SI). When tensile stress is applied to the nanowire, the Raman peak position decreases, compared with the unstrained value, to a value of (208.5 ± 1) cm^{-1}. Below this threshold, a discontinuity is observed, and the phonon energy undergoes a sudden increase of 5 cm^{-1}. When the nanowire is brought back to unstrained conditions, the phonon energy measured from Raman spectroscopy reaches a value of (216.5 ± 0.5) cm^{-1}. This value, slightly larger than the one measured in unstrained condition, hints at the presence of residual compressive stress in the nanowire. The discontinuity in phonon energy upon the application of tensile stress has been observed in several devices at values around (208.5 ± 1) cm^{-1} and can be attributed to the mechanical failure of the nanowire due to tensile stress. This hypothesis is confirmed by scanning electron microscopy (SEM) images of the devices taken after the strain cycle (see the SI).

Figure 2b shows the evolution of the electrical transport properties of the InAs nanowire. When compressive stress is applied, the four-probe resistance (shown in blue), the two-probe resistance measured at the voltage probes (shown in green), and the two-probe resistance measured at the current injectors (shown in red) increase by more than 2 orders of magnitude. When the device is brought back to unstrained conditions, the resistances return to their unstrained values. When subsequently tensile stress is applied to the nanowire and the TO phonon energy shifts below (214.9 ± 0.9) cm^{-1}, one of the current injection contacts fails, and the four-probe resistance of the nanowire device cannot be characterized further. However, the two-probe resistance can still be measured using the voltage probes. As more tensile stress is applied, the nanowire resistance decreases further by almost a factor of 6, and the TO phonon energy reaches (211.2 ± 0.8) cm^{-1}. Further tensile stress leads to a failure of the voltage probes, and the electrical characteristics of the device can no longer be obtained.

Figure 3a summarizes the measurement performed on two InAs nanowires, indicated with circles and squares. The four-probe resistance and the two-probe resistances are plotted as a function of the InAs TO phonon energy (top axis). The axial strain applied to the nanowire (bottom axis) can be determined from the TO phonon energy measured by Raman spectroscopy, as described in the SI. It can be shown that uniaxial stress breaks the symmetry of the crystal and the degeneracy between TO phonons. The TO phonon with atomic displacement along the strain direction (A1 symmetry,[63] labeled as TO_S) has the highest optical coupling, scattering intensity, and phonon energy shift with stress.[50] Using a bulk-like lattice dynamics model[67] and bulk values for the compliance tensor and for the

DOI: 10.1021/acs.nanolett.6b05098
Nano Lett. 2017, 17, 2816−2824

hydrostatic and deviatoric mode-Grüneisen parameters,[65] we estimate that the TO_S energy shift between (208.5 ± 1) cm^{-1} and (222.6 ± 0.6) cm^{-1} corresponds to axial strain ranging between −2.5% in compression and 2.1% in tension. This range is in very good agreement with measurements performed on GaAs nanowires on an equivalent bending mechanical device[50] and confirms the accuracy of the strain values extracted.

Figure 3a shows that the two-probe conductance measured at the voltage probes and the four-probe conductance have similar values across the entire stress range for both devices and follow the same functional dependence on strain. This observation confirms that the variation in the resistance of the metal−semiconductor interface is negligible and that the measured change in conductivity is to be attributed to changes in the transport properties of the InAs nanowire. This remarkable change in conductance induced by strain on the InAs nanowire can be understood by using a simple Drude model for conduction in a semiconductor. By differentiation, we can express the relative change in the conductance G of the nanowire as a sum of three contributions:

$$\frac{\delta G}{G} = (1 - 2\nu)\frac{\delta l}{l} + \frac{\delta \mu}{\mu} + \frac{\delta n}{n} \tag{1}$$

where we have expressed the mobility with μ, the charge carrier concentration with n, the nanowire Poisson ratio with ν, and the length as l. The first contribution, $(1 - 2\nu)\frac{\delta l}{l}$, captures the changes in the nanowire length and cross-section induced by strain. Its contribution to the relative change in conductance is of a few percent, i.e., of the same order of magnitude as the induced strain. The second contribution, $\frac{\delta \mu}{\mu}$, is related to strain-induced variation of the scattering time τ and of the effective mass m^*, according to the following equation:

$$\frac{\delta \mu}{\mu} = \frac{\delta \tau}{\tau} - \frac{\delta m^*}{m^*} \tag{2}$$

Both contributions are expected to be small and limited to few percent.[40,68] The last term, $\frac{\delta n}{n}$, captures the changes in charge-carrier concentration. We consider this term to be responsible to the large change in conductivity of the InAs nanowire upon strain. Given these considerations, we assume a constant value of mobility of 2000 $cm^2/(V\ s)$, typical for the nanowires used in this measurement,[69] and determine the average charge-carrier concentration in the nanowire cross section, shown in the left axis in Figure 3a. The increase in carrier concentration is 0.4 decade/% upon tensile stress and 1.7 decade/% upon compressive stress. The corresponding gauge factor, which is defined by

$$\mathrm{GF} = \frac{1}{R}\frac{\Delta R}{\varepsilon}$$

ranges between 48.8, when maximum tensile strain is achieved, and 7875, when measured upon maximum compression.

To gain an understanding of the physics of the charge modulation, we describe the strain dependence of the band extrema of InAs with an 8 band k·p model (for details, see the SI). The expected energy-level shifts are plotted in Figure 3b. The valence band degeneracy between a light hole and a heavy hole is lifted because of the symmetry-breaking shear deformation of the InAs unit cell. In contrast, the conduction band will shift because of the volume-changing isotropic deformation component of the strain tensor. The conduction band minimum (represented in green) and the heavy-hole maximum (represented in red) shift linearly with strain with slopes of opposite sign, whereas the light-hole band (represented in blue) follows a quadratic behavior because of the strain-mediated spin−orbit interaction and mixing with the split-off band (represented in yellow). In a first approximation, we use this band structure model, neglect the effect of surface accumulation and assume thermal equilibrium to infer the position of the Fermi level and the bulk electron concentration as a function of strain and doping concentration. However, this simplified model predicts the change in electron concentration to span only 2 orders of magnitude for stresses in the range between +2% and −2%. If the doping concentration is higher than the intrinsic carrier concentration, the modulation of the free electron concentration is reduced even further (more information about this is given in the SI). To confirm whether the degradation of the piezo-resistive coefficient with increasing doping concentration can be observed experimentally, we have performed measurements on Sn-doped nanowires with an electron concentration above 10^{18} cm^{-3} (details in the SI). However, these measurements yielded the same stress dependence and modulation of the conductance as observed in unintentionally doped nanowires. Thus, we conclude that the strain modifies the energy of the surface states and the surface accumulation on the nanowire. Only this effect can explain a change in electron concentration over 4 orders of magnitude, independently of the doping concentration.

To validate this hypothesis, we self-consistently modeled the effect of strain on the surface states and on the electrostatics of the strained InAs nanowire using TCAD.[70] InAs (110) surfaces are known to undergo a relaxation process that leads to donor-type surface states close to the valence band edge and acceptor-type states above the conduction band edge.[31] We therefore describe the surface state density with two Gaussian distributions for acceptor- and donor-type defects, with peak density of 3×10^{13} cm^{-2} and a full width at half-maximum of 480 meV.[28] Using this model, we fitted the nanowire electron concentration dependence on strain. The resulting fit of the experimental data is shown in Figure 3a as a black solid curve. The estimated shifts in energy of the donor and acceptor interface state distributions are shown in Figure 3b. In unstrained conditions, the acceptor traps are predicted to be located 300 meV above the conduction band minimum. This energy difference decreases to 176 meV upon 2% of compressive axial strain and increases to 424 meV when 2% tensile strain is induced on the nanowire. In contrast, the donor traps are predicted to have their maximum at the valence band edge in unstrained conditions, to shift by 193 meV below the valence band maximum (light hole band) upon 2% of compressive axial strain, and to 55 meV above the valence band maximum (heavy hole band) upon 2% of tensile strain. The energy shift induced by strain for the acceptor traps, also called acceptor trap deformation potential, is estimated to be 32 meV/% (taking the conduction band as energy reference, the deformation potential has a value of 62 meV/%). The strain-induced energy shift for the donor traps, i.e., the donor trap deformation potential, is estimated to be 62 meV/% (taking the conduction band as energy reference, the deformation potential has a value of 92 meV/%). Ab initio simulations confirm the correctness of these values (see details in the SI).

The observed modulation of the electron concentration with strain can be explained by considering the strain dependence of

DOI: 10.1021/acs.nanolett.6b05098
Nano Lett. 2017, 17, 2816−2824

the energy difference between trap states and the Fermi level, which shifts by 44 meV/%, the number of occupied trap states as a function of strain, and the effect that these states have on the device electrostatics. The acceptor states with energy higher than the Fermi level are occupied and neutral, and those with energy lower than the Fermi level acquire a negative charge, donating holes to the bulk InAs. With increasing compressive stress, the energy difference between the Fermi level and the average acceptor state energy decreases, and more acceptor traps become negatively charged. Such a negative charge at the surface of the nanowire acts like a negatively biased gate, induces the depletion of electrons from the nanowire surface, and reduces the electron concentration in the nanowire below the background doping, as shown in Figure 3c. The influence of donor-like surface states has also to be considered. Whereas donor states with an energy lower than the Fermi level are occupied and neutral, the donor state with an energy higher than the Fermi level become positively charged and donate electrons to the InAs nanowire. When applying tensile stress, the energy difference between the Fermi energy and the average donor-like state energy decreases. This causes a larger portion of donor states distribution to become ionized and contribute with more electrons to the conductivity of the nanowire. Such an increase in electron concentration of the nanowire upon tensile stress is captured by the TCAD simulation and shown in Figure 3e. Because of the effect of donor surface states, the electron concentration increases above the *n*-type background doping of 1×10^{16} cm^{-3}, suggesting that the donor surface states act as extrinsic dopants. These results demonstrate how uniaxial stress can affect the energy of surface traps and significantly modulate the electron concentration in the nanowire.

Conclusion and Outlook. In conclusion, we have investigated the effect of tensile and compressive uniaxial stress on the surface states and surface accumulation of InAs nanowires. Raman spectroscopy was performed to accurately gauge the strain induced on the device. Using the energy shift of the TO_S phonon as strain gauge (between 209 and 222 cm^{-1}), an axial strain ranging between −2.5% in compression and 2.1% in tension was estimated.

Four-probe and two-probe resistances of InAs nanowires were characterized as a function of stress. While changes in the contact resistance induced by stress were found to be negligible, the value of the four-probe resistances is found to modulate by strain over 4 orders of magnitude from tension to compression. The change in charge-carrier concentration is identified as being the main cause for the modulation of the nanowire conductivity, and its dependence on stress was simulated by a TCAD model. The energies of acceptor-type and donor-type interface states were deduced, and the deformation potentials for interface states were quantified. The acceptor trap deformation potential is estimated to be 32 meV/%, whereas the donor trap deformation potential is 62 meV/%. Finally, observations realized on InAs devices with different *n*-type doping concentrations and ab initio simulation confirmed the validity of the model.

These results provide a demonstration of the potential of strain technology for modifying surface states. Strain technology could be used together with passivation to control the density and the energetics of surface states. Notably, strain could be leveraged to shift the density of interface states into a range of energy in which device performance is not negatively affected, thus improving the performance of the device. Interface engineering and strain could be also used together, instead of doping, to control the charge-carrier concentration in ultrascaled devices. In this way, the limitations induced by random dopant fluctuations and doping deactivation at the nanoscale can be relaxed.[71] Finally, we envision that a systematic application of this methodology to devices based on other III–V semiconductor as well as other novel materials will provide new insights into the physics of surface states and help broaden the scope of strain as a technology booster.

Methods. *Nanowire Growth.* The nanowires are grown by the vapor–liquid–solid (VLS) method on an InAs (111) substrate (details about their crystal structure are given in the SI). The wafer surface is cleaned with a diluted hydrofluoric acid (DHF) diluted in ratio 20:1 in deionized water (DI). The surface is then rinsed in DI. Gold nanoparticles, diluted 1:2 in DI, are dispersed on the substrate and act as catalysts of the growth. Nanoparticle adhesion is ensured by dipping the substrate into a solution containing poly-L-lysine and rinsing in DI prior to deposition. The nanowires are grown by metal–organic vapor phase epitaxy (MOVPE). Trimethylindium and tertiarybutylarsine are used as metal–organic precursors, with flows of 1.4 μMol/min and 20 μMol/min, respectively. During growth, the temperature is kept at 430 °C. The effect of uniaxial stress for *n*-type doped InAs nanowires was studied on nanowires grown at the same temperature using trimethylindium, tertiarybutylarsine, and tetraethyltin, with flows of 2 μMol/min, 20 μMol/min, and 0.06 μMol/min, respectively. Both nanowire types have a diameter of 80 nm. After growth, the nanowires are coated with an Al_2O_3 shell of 5 nm thickness by atomic layer deposition (ALD).

Sample Fabrication. The nanowires are transferred from the growth chip to the flexible substrate by a dry process. Using a high-magnification optical microscope, individual nanowires are identified, and images are acquired to measure their position in relation to predefined markers. The metal contacts are fabricated by electron-beam lithography and lift-off technique. After lithography and development, but prior to metal deposition, the Al_2O_3 passivation shell is removed in buffered oxide etch (BOE). To ensure a reliable electrical contact with the metal, a long BOE etching time is used. In this step, the Al_2O_3 shell is etched from the entire section of the nanowire covered by the PMMA. Thus, the nanowire surface is exposed to ambient without passivation during measurement. A film of 80 nm of nickel and 40 nm of gold is used to establish the electrical contact to the InAs nanowire device. The contact areas between the metal and the nanowire have a minimum width of 300 nm and are spaced 700 nm apart between the voltage probes and 250 nm apart between the voltage probe and the current injector.

Raman Spectroscopy. Raman spectra are measured using a commercial Raman microscope (Horiba Scientific LabRam HR). The light of a frequency-doubled Nd:YVO_4 laser (Laser Quantum torus 532) with a wavelength of 532 nm is focused onto the central segment of the InAs nanowire device under test. The polarization of the excitation light is linear and aligned parallel to the nanowire axis. A laser power of 500 μW is used to minimize the heating of the nanowire and to achieve a good signal-to-noise ratio. A 100× long-working distance objective (working distance of 3.4 mm, numerical aperture of 0.8) is used to focus the excitation light into a spot of less than 1 μm (full-width half-maximum, fwhm) and to collect the scattered light in backscattering geometry. The scattered light is collected by a single-stage confocal spectrometer (1800 lines per mm grating)

DOI: 10.1021/acs.nanolett.6b05098
Nano Lett. 2017, 17, 2816–2824

equipped with a liquid-nitrogen-cooled silicon charge-coupled device (Horiba Symphony II). The polarization of the light collected by the spectrometer is not selected.

Electrical Characterization. After acquisition of the Raman spectrum, a set of electrical characteristics are measured in the absence of any laser excitation or white-light illumination for imaging. Electrical transport measurements are performed using a semiconductor parameter analyzer (Agilent 4155C). The devices under test are selected using a Keithley 707A switching matrix. The transport characteristics of each pair of contacts are measured at a low bias of 50 mV. These measurements are used to identify which contacts function correctly and for which stress range. A four-probe $I-V$ characteristics is then measured at a bias up to 400 mV. A current compliance of 10 μA is used to limit heating and possible contact failure upon tension. Two external contacts are connected to two source measurement units (SMU) configured as voltage source and ground, respectively, whereas the inner contacts are connected to two SMU configured as a zero-current source. This setup allows us to quantify the four-probe resistance as well as the two-probe resistance of the nanowire measured from the current injectors. Finally, a two-probe $I-V$ characteristics is measured at a bias up to 400 mV. The measurement is performed by applying a voltage bias across the two inner contacts, while the outer contacts are left floating. As was done for the four-probe measurement, a current compliance of 10 μA is used to limit heating and possible contact failure upon stress.

TEM Cross-Section Preparation, Imaging, and Analysis. The contact area between the InAs nanowire and the metal is investigated by cross-sectional STEM. The lamella was prepared by means of a FEI Helios Nanolab 450S focused ion beam (FIB). Before milling, a platinum layer of about 100 nm was deposited on the nanowire to prevent contamination and damage by the gallium ion beam. The lamella was thinned to less than 100 nm, inspected with a double spherical aberration-corrected JEOL JEM-ARM200F microscope operated at 200 kV, and equipped with a JEOL Dry SD100GV silicon drift detector with 100 mm^2 detection area for EDS analysis. In STEM mode, a convergence semiangle of 25 mrad was used in combination with an annular dark field (ADF) detector with inner and outer collection semiangles of 90 and 370 mrad, respectively.

TCAD Modeling. Assuming a mobility of 2000 $cm^2/(V\ s)$, typical for the nanowires used in this measurement,[69] and using the geometrical dimensions of the central section of the nanowire as obtained by SEM imaging of the device (diameter of 80 nm and length of 700 nm), we infer the charge carrier concentration in the nanowire using Sentaurus Device.[70] We define the nanowire geometry with a hexagonal cross section and a diagonal of 80 nm. The background doping in the bulk nanowire is assumed to be n-type, with a doping density of 1×10^{16} cm^{-3}. As the hole mobility is approximately 2 orders of magnitude smaller than the electron mobility in bulk InAs, the influence of holes has been ignored. The band structure parameter dependence on strain is obtained by the $k \cdot p$ model and provided as input to the TCAD tool. The position of the Fermi energy is determined by imposing global charge neutrality as well as the self-consistent solution of the Poisson equation. The interface trap density was defined by the sum of two contributions,[31] i.e., one acceptor-type defect distribution with an average energy higher than the conduction band edge, and one donor-type defect distribution, with an average energy close to the valence band edge. Both interface state densities have a Gaussian distribution in energy, with a maximum density of 3×10^{13} cm^{-2} eV^{-1} and a fwhm of 480 meV.[28] In the first optimization step, performed in unstrained conditions, the average energy of the acceptor and donor surface state distributions are used as fitting parameters to minimize the difference between the simulated and the measured electron concentration. To fit the strain dependence of the electron concentration, the average energy of the surface states is forced to shift linearly with strain, and the surface-state deformation potentials, which describe the energy shift of the surface states with strain, are used as fitting parameters.

■ ASSOCIATED CONTENT

Supporting Information

The Supporting Information is available free of charge on the ACS Publications website at DOI: 10.1021/acs.nanolett.6b05098.

> STEM imaging and crystal structure analysis of an InAs nanowire, cross-sectional STEM imaging and chemical analysis of the InAs/Nickel contact, four-probe electrical-measurement traces as function of strain, analysis of the Raman Spectra of an InAs device during a stress cycle, SEM image of an InAs nanowire device after a stress cycle, optical phonon dependence on strain in InAs, uniaxial stress effect on the Fermi level and the electron concentration of InAs, influence of interface states and strain-induced polarization charges on the electrical transport of a metal-semiconductor interface, electrical characterization of InAs nanowires as function of stress for different diameters and doping concentrations, ab-initio simulation of the uniaxial stress effect on the surface states of InAs (110) (PDF)

■ AUTHOR INFORMATION

Corresponding Author

*E-mail: giorgio.signorello@gmail.com.

ORCID

G. Signorello: 0000-0001-7066-0416

H. Schmid: 0000-0002-0228-4268

Author Contributions

G.S., H.S., and H.R. conceived the idea of the experiment; G.S. designed and realized the experimental setup; G.S., M.S., and U.D. designed and fabricated the substrates; G.S. and M.S. fabricated the devices and performed the measurements; N.B. and M.R. analyzed the samples with TEM; G.S. performed the band structure and analytical modeling; G.S., S.S., and S.W. interpreted the data; S.S. and A.S. performed the TCAD modeling; G.S., S.S., and H.R. wrote the manuscript; all authors discussed and contributed to the manuscript.

Notes

The authors declare no competing financial interest.

■ ACKNOWLEDGMENTS

We acknowledge Hans Ruedi Steinauer, Marcel Bürge, Ralph Heller, Patrik Zellekens, and Jonas Weiss for their contributions to the experimental method and setup, Bernd Gotsmann, Veeresh Deshpande, Lukas Czornomaz, Mathieu Luisier, Johannes Gooth, Benedikt Mayer, and Walter Riess for scientific discussions. The research leading to these results has received funding from the European Union Seventh Framework Program (FP7/2007-2013) E2Switch under

Grant Agreement No. 619509, ICT-2013-11 IIIVMOS under Grant Agreement No. 619326, from the European Union Horizon 2020 Framework Program (H2020-MSCA-IF-2015) MODES under Grant Agreement No. 704045, and by the Swiss National Science Foundation under project number 200021_156746.

■ REFERENCES

(1) Del Alamo, J. A. *Nature* **2011**, *479*, 317−323.
(2) Theis, T. N.; Solomon, P. M. *Science* **2010**, *1600*, 10−12.
(3) Ionescu, A. M.; Riel, H. *Nature* **2011**, *479*, 329−337.
(4) Ford, A. C.; Ho, J. C.; Chueh, Y.-L.; Tseng, Y.-C.; Fan, Z.; Guo, J.; Bokor, J.; Javey, A. *Nano Lett.* **2009**, *9*, 360−365.
(5) Ko, H.; Takei, K.; Kapadia, R.; Chuang, S.; Fang, H.; Leu, P. W.; Ganapathi, K.; Plis, E.; Kim, H. S.; Chen, S.-Y.; Madsen, M.; Ford, A. C.; Chueh, Y.-L.; Krishna, S.; Salahuddin, S.; Javey, A. *Nature* **2010**, *468*, 286−289.
(6) Chang, L.; Frank, D. J.; Montoye, R. K.; Koester, S. J.; Ji, B. L.; Coteus, P. W.; Dennard, R. H.; Haensch, W. *Proc. IEEE* **2010**, *98*, 215−236.
(7) Liang, D.; Bowers, J. E. *Nat. Photonics* **2010**, *4*, 511−517.
(8) Wang, Z.; Tian, B.; Pantouvaki, M.; Guo, W.; Absil, P.; Van Campenhout, J.; Merckling, C.; Van Thourhout, D. *Nat. Photonics* **2015**, *9*, 837−842.
(9) Chen, S.; Li, W.; Wu, J.; Jiang, Q.; Tang, M.; Shutts, S.; Elliott, S. N.; Sobiesierski, A.; Seeds, A. J.; Ross, I.; Smowton, P. M.; Liu, H. *Nat. Photonics* **2016**, *10*, 307−311.
(10) Offermans, P.; Crego-Calama, M.; Brongersma, S. H. *Nano Lett.* **2010**, *10*, 2412−2415.
(11) Du, J.; Liang, D.; Tang, H.; Gao, X. P. A. *Nano Lett.* **2009**, *9*, 4348−4351.
(12) Karg, S. F.; Troncale, V.; Drechsler, U.; Mensch, P.; Das Kanungo, P.; Schmid, H.; Schmidt, V.; Gignac, L.; Riel, H.; Gotsmann, B. *Nanotechnology* **2014**, *25*, 305702.
(13) Wu, P. M.; Gooth, J.; Zianni, X.; Svensson, S. F.; Gluschke, J. G.; Dick, K. A.; Thelander, C.; Nielsch, K.; Linke, H. *Nano Lett.* **2013**, *13*, 4080−4086.
(14) Roulleau, P.; Baer, S.; Choi, T.; Molitor, F.; Güttinger, J.; Müller, T.; Dröscher, S.; Ensslin, K.; Ihn, T. *Nat. Commun.* **2011**, *2*, 239.
(15) Blömers, C.; Lepsa, M. I.; Luysberg, M.; Grützmacher, D.; Lüth, H.; SchäPers, T. *Nano Lett.* **2011**, *11*, 3550−3556.
(16) Heedt, S.; Morgan, C.; Weis, K.; Bürgler, D. E.; Calarco, R.; Hardtdegen, H.; Grützmacher, D.; SchäPers, T. *Nano Lett.* **2012**, *12*, 4437−4443.
(17) Pfund, A.; Shorubalko, I.; Ensslin, K.; Leturcq, R. *Phys. Rev. Lett.* **2007**, *99*, 36801.
(18) Mourik, V.; Zuo, K.; Frolov, S. M.; Plissard, S. R.; Bakkers, E. P. A. M.; Kouwenhoven, L. P. *Science* **2012**, *336*, 1003.
(19) Wang, C. H.; Wang, S. W.; Doornbos, G.; Astromskas, G.; Bhuwalka, K.; Contreras-Guerrero, R.; Edirisooriya, M.; Rojas-Ramirez, J. S.; Vellianitis, G.; Oxland, R.; Holland, M. C.; Hsieh, C. H.; Ramvall, P.; Lind, E.; Hsu, W. C.; Wernersson, L.-E.; Droopad, R.; Passlack, M.; Diaz, C. H. *Appl. Phys. Lett.* **2013**, *103*, 143510.
(20) Bryllert, T.; Wernersson, L.-E.; Löwgren, T.; Samuelson, L. *Nanotechnology* **2006**, *17*, S227−S230.
(21) Konar, A.; Mathew, J.; Nayak, K.; Bajaj, M.; Pandey, R. K.; Dhara, S.; Murali, K. V. R. M.; Deshmukh, M. M. *Nano Lett.* **2015**, *15*, 1684−1690.
(22) Dayeh, S. a.; Yu, E. T.; Wang, D. *Small* **2009**, *5*, 77−81.
(23) van Tilburg, J. W. W.; Algra, R. E.; Immink, W. G. G.; Verheijen, M.; Bakkers, E. P. A. M.; Kouwenhoven, L. P. *Semicond. Sci. Technol.* **2010**, *25*, 24011.
(24) Suzuki, R.; Taoka, N.; Yokoyama, M.; Lee, S.; Kim, S. H.; Hoshii, T.; Yasuda, T.; Jevasuwan, W.; Maeda, T.; Ichikawa, O.; Fukuhara, N.; Hata, M.; Takenaka, M.; Takagi, S. *Appl. Phys. Lett.* **2012**, *100*, 132906.
(25) Wieder, H. H. *Appl. Phys. Lett.* **1974**, *25*, 206−208.
(26) Spicer, W. E.; Lindau, I.; Skeath, P.; Su, C. Y. *J. Vac. Sci. Technol.* **1980**, *17*, 1019.
(27) Riel, H.; Wernersson, L.-E.; Hong, M.; del Alamo, J. A. *MRS Bull.* **2014**, *39*, 668−677.
(28) Brammertz, G.; Lin, H.-C. C.; Caymax, M.; Meuris, M.; Heyns, M.; Passlack, M. *Appl. Phys. Lett.* **2009**, *95*, 202103−202109.
(29) Mankefors, S.; Nilsson, P. O. *J. Phys.: Condens. Matter* **2001**, *13*, 823−832.
(30) Razavieh, A.; Mohseni, P. K.; Jung, K.; Mehrotra, S.; Das, S.; Suslov, S.; Li, X.; Klimeck, G.; Janes, D. B.; Appenzeller, J. *ACS Nano* **2014**, *8*, 6281−6287.
(31) Weber, J. R.; Janotti, A.; Van de Walle, C. G. *Appl. Phys. Lett.* **2010**, *97*, 192106.
(32) Mönch, W. *Semiconductor Surfaces and Interfaces*; Springer Series in Surface Sciences; Berlin, 2001; Vol. *26*.
(33) Jiang, X.; Xiong, Q.; Nam, S.; Qian, F.; Li, Y.; Lieber, C. M. *Nano Lett.* **2007**, *7*, 3214−3218.
(34) Affentauschegg, C.; Wieder, H. H. *Semicond. Sci. Technol.* **2001**, *16*, 708−714.
(35) Olsson, L.; Andersson, C.; Håkansson, M.; Kanski, J.; Ilver, L.; Karlsson, U. *Phys. Rev. Lett.* **1996**, *76*, 3626−3629.
(36) Noguchi, M.; Hirakawa, K.; Ikoma, T. *Phys. Rev. Lett.* **1991**, *66*, 2243−2246.
(37) Sun, Y.; Thompson, S. E.; Nishida, T. *J. Appl. Phys.* **2007**, *101*, 104503.
(38) Fischetti, M. V.; Laux, S. E. *J. Appl. Phys.* **1996**, *80*, 2234.
(39) Fischetti, M. V.; Gámiz, F.; Hänsch, W. *J. Appl. Phys.* **2002**, *92*, 7320.
(40) Nainani, A.; Yum, J.; Barnett, J.; Hill, R.; Goel, N.; Huang, J.; Majhi, P.; Jammy, R.; Saraswat, K. C. *Appl. Phys. Lett.* **2010**, *96*, 45−48.
(41) Suthram, S.; Sun, Y.; Majhi, P.; Ok, I.; Kim, H.; Harris, H. R.; Goel, N.; Parthasarathy, S.; Koehler, A.; Acosta, T.; Nishida, T.; Tseng, H.-H.; Tsai, W.; Lee, J.; Jammy, R.; Thompson, S. E. In *2008 Symposium on VLSI Technology*; IEEE, 2008; pp 182−183.
(42) Chu, M.; Sun, Y.; Aghoram, U.; Thompson, S. E. *Annu. Rev. Mater. Res.* **2009**, *39*, 203−229.
(43) Rossel, C.; Weigele, P.; Czornomaz, L.; Daix, N.; Caimi, D.; Sousa, M.; Fompeyrine, J. *Solid-State Electron.* **2014**, *98*, 88−92.
(44) Xia, L.; Del Alamo, J. A. *Appl. Phys. Lett.* **2009**, *95*, 243504.
(45) Lexholm, M.; Karlsson, I.; Boxberg, F.; Hessman, D. *Appl. Phys. Lett.* **2009**, *95*, 113103.
(46) Zhou, L. G.; Huang, H. *Appl. Phys. Lett.* **2004**, *84*, 1940−1942.
(47) Chen, C. Q.; Shi, Y.; Zhang, Y. S.; Zhu, J.; Yan, Y. J. *Phys. Rev. Lett.* **2006**, *96*, 75505.
(48) Nam, C.-Y.; Jaroenapibal, P.; Tham, D.; Luzzi, D. E.; Evoy, S.; Fischer, J. E. *Nano Lett.* **2006**, *6*, 153−158.
(49) Wang, Y.-B.; Wang, L.-F.; Joyce, H. J.; Gao, Q.; Liao, X.-Z.; Mai, Y.-W.; Tan, H. H.; Zou, J.; Ringer, S. P.; Gao, H.-J.; Jagadish, C. *Adv. Mater.* **2011**, *23*, 1356−1360.
(50) Signorello, G.; Karg, S.; Björk, M. T.; Gotsmann, B.; Riel, H. *Nano Lett.* **2013**, *13*, 917−924.
(51) Signorello, G.; Lörtscher, E.; Khomyakov, P. A.; Karg, S.; Dheeraj, D. L.; Gotsmann, B.; Weman, H.; Riel, H. *Nat. Commun.* **2014**, *5*, 3655.
(52) He, R.; Yang, P. *Nat. Nanotechnol.* **2006**, *1*, 42−46.
(53) Cao, J. X.; Gong, X. G.; Wu, R. Q. *Phys. Rev. B: Condens. Matter Mater. Phys.* **2007**, *75*, 3−6.
(54) Rowe, A. C. H. *Nat. Nanotechnol.* **2008**, *3*, 311−312.
(55) Lugstein, A.; Steinmair, M.; Steiger, A.; Kosina, H.; Bertagnolli, E. *Nano Lett.* **2010**, *10*, 3204−3208.
(56) Li, X.; Wei, X.; Xu, T.; Pan, D.; Zhao, J.; Chen, Q. *Adv. Mater.* **2015**, *27*, 2852−2858.
(57) Tuzzolino, A. J. *Phys. Rev.* **1958**, *112*, 30−30.
(58) Bir, G. L.; Pikus, G. E. *Symmetry and Strain-Induced Effects in Semiconductors*; Wiley, 1974.
(59) Bernal, R. A.; Filleter, T.; Connell, J. G.; Sohn, K.; Huang, J.; Lauhon, L. J.; Espinosa, H. D. *Small* **2014**, *10*, 725−733.
(60) Zhu, Y.; Espinosa, H. D. *Proc. Natl. Acad. Sci. U. S. A.* **2005**, *102*, 14503−14508.

DOI: 10.1021/acs.nanolett.6b05098
Nano Lett. 2017, 17, 2816−2824

(61) Zhu, Y.; Moldovan, N.; Espinosa, H. D. *Appl. Phys. Lett.* **2005**, *86*, 13506.
(62) Signorello, G.; Schraff, M.; Zellekens, P.; Drechsler, U.; Buerge, M.; Steinauer, H. R.; Heller, R.; Tschudy, M.; Riel, H. *arXiv* **2017**, 1704.01394 (submitted).
(63) Hörmann, N. G.; Zardo, I.; Hertenberger, S.; Funk, S.; Bolte, S.; Döblinger, M.; Koblmüller, G.; Abstreiter, G. *Phys. Rev. B: Condens. Matter Mater. Phys.* **2011**, *84*, 155301.
(64) Möller, M.; de Lima, M. M.; Cantarero, A.; Dacal, L. C. O.; Madureira, J. R.; Iikawa, F.; Chiaramonte, T.; Cotta, M. A. *Phys. Rev. B: Condens. Matter Mater. Phys.* **2011**, *84*, 85318.
(65) Cerdeira, F.; Buchenauer, C.; Pollak, F. F. H.; Cardona, M. *Phys. Rev. B* **1972**, *5*, 580.
(66) Aoki, K.; Anastassakis, E.; Cardona, M. *Phys. Rev. B: Condens. Matter Mater. Phys.* **1984**, *30*, 681−687.
(67) Ganesan, S.; Maradudin, A.; Oitmaa, J. *Ann. Phys.* **1970**, *56*, 556−594.
(68) Betti Beneventi, G.; Reggiani, S.; Gnudi, A.; Gnani, E.; Alian, A.; Collaert, N.; Mocuta, A.; Thean, A.; Baccarani, G. *IEEE Trans. Electron Devices* **2015**, *62*, 3645−3652.
(69) Ghoneim, H.; Mensch, P.; Schmid, H.; Bessire, C. D.; Rhyner, R.; Schenk, A.; Rettner, C.; Karg, S.; Moselund, K. E.; Riel, H.; Björk, M. T. *Nanotechnology* **2012**, *23*, 505708.
(70) Synopsys. *Sentaurus Devices User Guide*, 2013.
(71) Björk, M. T.; Schmid, H.; Knoch, J.; Riel, H.; Riess, W. *Nat. Nanotechnol.* **2009**, *4*, 103−107.

DOI: 10.1021/acs.nanolett.6b05098
Nano Lett. 2017, 17, 2816−2824